



An improved PET image reconstruction method based on super-resolution

Ying Wang^{a,b}, Xuezhu Zhang^c, Mengxi Zhang^c, Dong Liang^{a,d}, Xin Liu^{a,d}, Hairong Zheng^{a,d}, Yongfeng Yang^{a,d}, Zhanli Hu^{a,d,*}

^a Lauterbur Research Center for Biomedical Imaging, Shenzhen Institutes of Advanced Technology, Chinese Academy of Sciences, Shenzhen 518055, China

^b College of Electrical and Information Engineering, Hunan University, Changsha 410082, China

^c Department of Biomedical Engineering, University of California, Davis, CA 95616, USA

^d Chinese Academy of Sciences Key Laboratory of Health Informatics, Shenzhen 518055, China

ARTICLE INFO

Keywords:

Positron emission tomography
Reconstruction
Patch regularization
Penalized maximum likelihood
Random forests

ABSTRACT

Positron emission tomography (PET) is a non-invasive high-end examination that can quantitatively detect early disease stages. It complements information provided by functional and anatomical imaging. Therefore, PET is widely used clinically early on in the process of diagnosing malignant tumors or lesions. Fast and accurate reconstruction of PET images has been the subject of ongoing research. Patch-based regularization penalty likelihood reconstruction can reconstruct PET images more accurately, but it is sensitive to its algorithm's parameter values and requires a great deal of time to adjust parameters to achieve the best reconstruction. In this paper, we propose a novel method that uses random forests to improve PET imaging resolution at each iteration reconstruction step in the sinogram domain and the image domain; we refer to this method as patch-based super-resolution random forests reconstruction (patch-SRF). The patch-SRF algorithm allows the reconstruction to converge in advance and avoids the free-time adjustment process, achieving better reconstruction results despite relatively poor parameter settings.

1. Introduction

Positron emission tomography (PET) is a relatively advanced imaging technology that uses radioactive drugs (tracers) to illustrate tissue metabolism. It is commonly used in patients with cancer, neurological disease, or cardiac disease. Compared with other medical imaging technologies, such as X-ray computed tomography (CT) and magnetic resonance imaging (MRI), PET allows for an earlier diagnosis. Therefore, PET has important applications in medicine. However, PET has poorer spatial resolution than other imaging techniques. To address this issue, continuous research into PET imaging reconstruction technology has been and is being conducted. Improving the resolution of reconstructed PET images by improving detector width and various physical parameters (e.g., the scattering fraction, counting statistics, and positron range, etc.) is the most straightforward solution [1,2]. However, the cost of this solution is high. Therefore, improving PET image reconstruction algorithms to improve PET image quality has been the common approach.

In the past few decades, numerous efforts have been made to develop PET image reconstruction algorithms, including analysis and iterative reconstruction methods [3–5]. Filtered back-projection (FBP) reconstruction [3,6,7] is an example of a typical analytical method

that is designed to overcome the limitations of conventional back-projection by applying a convolution filter to remove blurring. The FBP reconstruction algorithm utilizes simple and fast calculations, but its reconstruction results have poor resolution and noise characteristics that require complete projection data and large count values. Using an iterative image reconstruction [7–9] method allows for the introduction of various physical imaging conditions and statistical models during the process of image reconstruction, and consequently can improve image quality and spatial resolution. It can also be applied to situations with incomplete projections.

At present, iterative image reconstruction methods mainly utilize algebraic iterative reconstruction algorithms based on algebraic equation theory and statistical iterative reconstruction algorithms based on various statistical criteria. Statistical iterative reconstruction algorithms are more widely used and mainly include image reconstruction methods based on the least square error estimations [10–12] and on maximum likelihood (ML) estimations [13–16]. Bayesian image reconstruction methods are mainly based on maximum a posteriori estimations (MAP) [17–21]. The disadvantage of the least square error estimation is that it does not properly take into account the statistical properties of the projection data. Although the least square error estimation is the best estimate of data obeying a Gaussian distribution,

* Corresponding author at: Lauterbur Research Center for Biomedical Imaging, Shenzhen Institutes of Advanced Technology, Chinese Academy of Sciences, Shenzhen 518055, China.

E-mail address: zl.hu@siat.ac.cn (Z. Hu).

the pixel density data of positron imaging is closer to the Poisson distribution. The maximum likelihood estimation reconstruction method estimates images from projections by maximizing the log likelihood of the PET projection data. It takes full advantage of the inherent resolution of the system because it takes into account the statistical properties of the data and thus obtains better reconstruction results; however, when the projection data contain relatively serious statistical noise, the quality of the reconstructed images degrades as the iterations proceed.

Recently, super-resolution (SR) has been widely used to improve PET image quality. The traditional SR method is based on interpolation [22,23] using bilinear, bicubic, nearest, and other interpolations. Traditional machine learning methods, such as sparse representation, [24,25], random forests [26–28], and the latest neural network technologies [29–31], have also been introduced into the SR field. We have previously applied the random forest SR algorithm to PET images [28] and found that this algorithm is superior to others in the PET field. In the current study we built on our previous work and apply the random forest algorithm to the PET SR reconstruction process.

We propose a novel algorithm called patch-SRF that combines penalty likelihood PET image reconstruction based on patch regularization with PET image super-resolution processing based on random forests. Patch-based regularization has recently greatly progressed in improving PET image quality. It preserves features and texture within patches, in addition to preserving edges. Furthermore, introducing a regularization term in the process of the image iterative update addresses the issue of image quality degradation resulting from the maximum likelihood estimation method's iterative process [32]. However, because patch-based regularization is sensitive to hyper-parameter values such as the counting rate, the regularization parameter that controls the shape of the penalty function, it can require a great deal of time to adjust the parameters to achieve the best reconstruction. To overcome these limitations, we utilize a super-resolution procedure that directly learns the mapping from low-resolution (LR) to high-resolution (HR) reconstructed PET image patches or projection image patches for each iteration using random forests. The addition of the SR process allows the reconstruction to converge in advance. Overall, this method can avoid the free-time adjustment process and can achieve better reconstruction results under relatively poor parameter settings.

The remainder of the paper is organized as follows: in Section 2, we present the principles of penalty likelihood reconstruction based on patch regularization and the random forest algorithm; in Section 3, we present the experimental settings of the specific simulation; Section 4 details the results; finally, Section 5 presents a conclusion.

2. Methods

2.1. Patch-based penalty likelihood reconstruction

During a PET exam, radionuclides injected into the subject decay to produce positrons. The positron is annihilated by an electron of the surrounding material, and two back-to-back gamma rays are produced. The opposite detector pairs receive the pairs of back-to-back gamma photons within a given time difference, i.e., a coincident event is detected. The in-vivo image of the subject is reconstructed from the sum of the events, which is called sinogram y , and is detected by several detectors contained in the scanner ring.

Since the positron emission itself satisfies the Poisson distribution, we assume that the PET data sinogram y can be considered as a distribution of independent Poisson random variables. Based on the independent Poisson assumption, we can write the log likelihood function of y as

$$L(y|x) = \sum_{i=1}^{n_i} y_i \log \bar{y}_i - \bar{y}_i \quad s.t. \quad \bar{y} = Px + r + s \quad (1)$$

where the expected data $\bar{y} = \{\bar{y}_i\}$ is related to the unknown image x by the projective transform. n_i is the total number of detector pairs.

P is the system matrix representing the probabilities of detecting an event by detector pair i . r explains random background events, and s represents scatter events.

Penalized likelihood (PL) reconstruction estimates the unknown image x by maximizing a penalized likelihood function

$$\hat{x} = \underset{x \geq 0}{\operatorname{argmax}} \Phi(x), \quad \Phi(x) = L(y|x) - \beta U(x) \quad (2)$$

where $U(x)$ is a roughness function based on a patch, and β is the regularization parameter, which controls the trade-off between data fidelity and spatial smoothness.

In other words, we choose $Q_L(x; x^n)$ as the likelihood surrogate function, which is defined as

$$Q_L(x; x^n) = \sum_{j=1}^{n_j} p_j \left(\hat{x}_{j,EM}^{n+1} \log x_j - x_j \right) \quad (3)$$

where $p_j = \sum_{i=1}^{n_i} p_{ij}$,

$$\hat{x}_{j,EM}^{n+1} = \frac{x_j^n}{p_j} \sum_{i=1}^{n_i} p_{ij} \frac{y_i}{\bar{y}_i^n}, \quad \bar{y}^n = Px^n + r \text{ is the expected projection at iteration } n,$$

and n_j is the total number of pixels in an image.

We adopt the following separable surrogate function:

$$Q_U^b(x; x^n) = \frac{1}{2} \sum_{j=1}^{n_j} w_j^n \left(x_j - \hat{x}_{j,Reg}^{n+1} \right)^2 \quad (4)$$

where $\hat{x}_{j,Reg}^{n+1} = \frac{1}{2w_j^n} \sum_{k \in N_j} w_{jk} (x^n) \left(x_k^n + x_j^n \right)$,

$w_j^n = \sum_{k \in N_j} w_{jk} (x^n)$ is the pixel-wise weight, j denotes the patch $f_j(x)$,

and k denotes the patch $f_k(x)$.

Solving the Karush–Kuhn–Tucker (KKT) condition [33], we obtain the PL reconstructed image estimate at iteration $(n+1)$:

$$x_j^{n+1} = \frac{2\hat{x}_{j,EM}^{n+1}}{\sqrt{\left(1 - \beta_j^n \hat{x}_{j,Reg}^{n+1}\right)^2 + 4\beta_j^n \hat{x}_{j,EM}^{n+1}} + \left(1 - \beta_j^n \hat{x}_{j,Reg}^{n+1}\right)} \quad (5)$$

where $\beta_j^n = \frac{\beta w_j^n}{p_j}$. The above updated equation approaches the ML-EM estimate when β goes to zero.

2.2. Random forests

To enhance the image quality usually obtained from a patch-based regularization reconstruction, we have introduced a model based on random forests. More specifically, we chose this approach so that images reconstructed from each iteration would selectively undergo super-resolution processing.

Random forests are a combination of tree predictors where each tree depends on the values of a random vector sampled independently; all the trees in the forest have the same distribution [26]. Every decision tree in the random forest is independently trained, and the training set is randomly sampled with putting back from the original training samples $\{x_H^n, x_L^n\}$, where x_L is the input LR label space, and x_H is the output feature space. The decision tree is a binary tree that learns the mapping relationship matrix W from the input LR label space x_L to output HR space x_H . To train N decision trees, we use the bootstrapping method [34] to randomly return the same size training samples for N times.

Each tree T_l independently and recursively separates the data space into left and right disjoint cells, which ultimately correspond to a number of leaf nodes. This separation defines the mapping matrices W which is learned from our data; each leaf l can learn a linear model

$$m_l(x_L) = \sum_{j=0}^J W_j^l \cdot \phi_j(x_L) \quad (6)$$

where the leaf model finds the data dependence regression matrices $W_j(x_L)$ for all basis functions $\phi_j(x_L)$, which can represent various functions, such as linear, polynomial and constant functions. $\gamma + 1$ is the number of types of base functions. In this problem, we choose the commonly used linear function ($\phi_j(x_L) = x_L$).

To find all W_j^l values, we followed the principle of the regularized least squares error, which can be performed as follows:

$$\operatorname{argmin}_{W(x_L)} \|x_H - W^l(x_L) \cdot \Phi(x_L)\|_2^2 \quad (7)$$

where we stacked all W_j^l values and the data into matrices W^l , $\Phi(x_L)$, and x_H . According to the ridge regression, the regression coefficient is calculated as $W^{lT} = (\Phi(x_L)^T \Phi(x_L) + \lambda I)^{-1} \Phi(x_L)^T \cdot x_H$. λI is the regularization term, where I is the identity matrix, and λ is the regularization parameter, which is set in advance.

Because the above allows us to know the model of every tree, we then only need to average the predicted values from all the decision trees to obtain the final prediction. The SR prediction result is as follows:

$$\bar{x} = \frac{1}{T} \sum_{t=1}^T m_{l(t)}(x_L) = \frac{1}{T} \sum_{t=1}^T \sum_{j=0}^{\gamma} W_j^l \cdot \phi_j(x_L) \quad (8)$$

where $l(t)$ is the leaf node of tree t from which sample x_L is split, and T is the total number of trees.

2.3. Proposed method

The optimization algorithm uses super-resolution processing at each reconstruction iteration step, whether in both the sinogram domain and/or the image domain. SR processing in the sinogram domain compensates for sinogram y^n before the expectation maximization (EM) update. The image domain consists of the reconstructed image estimations from super-resolution processing after each iteration through the learned random forest model. When the maximum number of iterations is achieved, the whole iteration scheme stops. The pseudo code of the super-resolution iterative reconstruction, which is referred to as patch-SRF, is summarized in Algorithm 1.

3. Experiment

3.1. Experimental setup

To validate the proposed algorithm, we performed three sets of simulation experiments with different count levels. The first set had a count level equal to 50k and performed 100 iterations, the second set performed the same number of iterations with a count level equal to 200k, and the last set performed 50 iterations with a count level equal to 3M. A total of 20 experiments were simulated at each count level, and each was reconstructed independently for statistical comparisons. The quantitative results for each set of experiments presented in the paper are the averages of the 20 experiments.

The experimental data were obtained from Wuhan Tongji Hospital and were collected from a Discovery PET/CT 690 scanner (GE, city, state, country). Multiple axial whole-body PET attenuation-corrected images were selected for the iterative reconstructions. The sinogram and iterative image results of each iteration process were used as low-resolution samples in the training set of the super-resolution model. The reference sinogram and original image served as corresponding high-resolution samples. Super-resolution iterative reconstructions were then performed with different counting levels and compared with the corresponding iterative reconstruction results that had not undergone super-resolution processing, but had the same count levels and the numbers of iterations. All the experiments were conducted in MATLAB 2016b under Ubuntu 18.04 on a PC with an Inter(R) Core (TM) 3.60 GHz CPU and 16 GB of RAM.

Table 1

PSNR and SSIM values of the whole image and the three ROIs (outlined by red dotted squares in Fig. 1(g)).

| | Patch (PSNR/SSIM) | Patch-SRF (PSNR/SSIM) |
|-------|-------------------|-----------------------|
| Whole | 29.67/0.87 | 34.51/0.88 |
| ROI 1 | 29.37/0.86 | 33.45/0.89 |
| ROI 2 | 21.36/0.86 | 26.95/0.86 |
| ROI 3 | 18.68/0.91 | 24.88/0.93 |

3.2. Quantitative assessment

To quantitatively evaluate the performance of the proposed algorithm, two standard metrics which are widely used in image quality evaluations, were compared: PSNR and SSIM.

The peak signal-to-noise ratio (PSNR) [28] is the most common and widely used objective measurement for evaluating image quality and is calculated as follows:

$$\text{PSNR} = 10 \log_{10} \frac{\max(u_n, u_{\text{original}_n})^2}{\frac{1}{N} \sum_{n=1}^N (u_n - u_{\text{original}_n})^2} \quad (9)$$

where u_n and u_{original_n} are the pixel values of the reconstructed image and the original reference image, respectively, and N is the total number of pixels in the reconstructed image. Larger PSNR values indicate less the distortion and thus better image quality.

The structural similarity index (SSIM) [28] reflects the properties of the object structure and measures the similarity of the two images. The formula is defined as follows:

$$\text{SSIM} = \frac{2\bar{u}_{\text{original}}\bar{u}(\sigma_{u_{\text{original}}u} + c_2)}{(\bar{u}_{\text{original}}^2 + \bar{u}^2 + c_1)(\sigma^2 + \sigma_{\text{original}}^2 + c_2)} \quad (10)$$

where $\bar{u}_{\text{original}}$ and $\sigma_{u_{\text{original}}}$ denote the mean value and variance of the original reference image x , respectively. Similarly, \bar{u} and σ are the mean value and variance of the reconstructed image \hat{x} , respectively. $\sigma_{u_{\text{original}}u}$ is the covariance of the reference and the reconstructed image. c_1 and c_2 are constants used to maintain stability. The SSIM value ranges from zero to one; as the two images approach being identical, the SSIM value approaches one.

4. Results

The experimental results are shown in Fig. 1. Fig. 1(a)–(c) are the results at a count level of 50k and consist of the reference image, the patch reconstruction, and the result of the proposed method, respectively. Fig. 1(d)–(f) are the comparison results at a count level of 200k, and Fig. 1(g)–(i) correspond to the comparison results at a count level of 3M. By looking at the regions indicated by the red arrows, we can see that the image reconstructed by the proposed algorithm is significantly better than the patch reconstruction. Fig. 2 shows a partially enlarged view of Fig. 1(g)–(i), corresponding to the three areas outlined by red dotted boxes in Fig. 1(g). In the partially enlarged view, the differences between the three sets become more apparent. The image reconstructed by the proposed algorithm is significantly better than the patch-based regularization penalty likelihood reconstruction method.

The quantitative values, including PSNR and SSIM, of the whole image and the three ROIs are shown in Table 1, which shows that the image reconstructed by the proposed algorithm has significantly higher PSNR and SSIM values than the patch reconstruction method, indicating superior image quality. A profile comparison of the 3M count level results, corresponding to the position of the black line in Fig. 1(g), is shown in Fig. 3, which displays profile information of three images. The residual images of the patch reconstruction and the proposed algorithm at a 3M count level are displayed in Fig. 4. Fig. 4(a) is the residual image of the reference and the patch results, and Fig. 4(b) is the residual image of the reference and the results of the proposed algorithm. We can see a noticeable difference in the areas indicated by the red arrows. The reconstructed PET image has superior image

Algorithm 1. PET image reconstruction algorithm based on patch-based regularization and super-resolution forests (patch-SRF algorithm)

1. Initialize parameters: maximum number of iterations (maxiter), regularization parameter β , and SRF parameters, the number and maximum depth of trees;
Initialize image: $\mathbf{x}_j^1 = \mathbf{1}$;
 2. For $n=1$ to maxiter do
 3. Super-resolution processing for sinogram: $\bar{\mathbf{y}}_i^n = \mathbf{W}(\mathbf{y}_i^n)\mathbf{y}_i^n$
 4. EM image update from sinogram $\{\mathbf{y}_i\}$: $\hat{\mathbf{x}}_{j,EM}^{n+1} = \frac{\mathbf{x}_j^n}{p_j} \sum_{i=1}^{n_i} p_{ij} \frac{y_i}{\bar{y}_i^n}$
 5. Image smoothing: $\hat{\mathbf{x}}_{j,Reg}^{n+1} = \frac{1}{2w_j^n} \sum_{k \in N_j} w_{jk}(\mathbf{x}_k^n + \mathbf{x}_j^n)$
 6. Pixel-by-pixel image fusion: $\mathbf{x}_j^{n+1} = \frac{2\hat{\mathbf{x}}_{j,EM}^{n+1}}{\sqrt{(1-\beta_j^n \hat{\mathbf{x}}_{j,Reg}^{n+1})^2 + 4\beta_j^n \hat{\mathbf{x}}_{j,EM}^{n+1} + (1-\beta_j^n \hat{\mathbf{x}}_{j,Reg}^{n+1})}}$
 7. Super-resolution (SR) model: $\hat{\mathbf{x}}_j^{n+1} = \mathbf{W}(\mathbf{x}_j^{n+1})\mathbf{x}_j^{n+1}$
 8. End the loop
 9. Return the reconstructed image $\hat{\mathbf{x}}^{n+1}$.
-

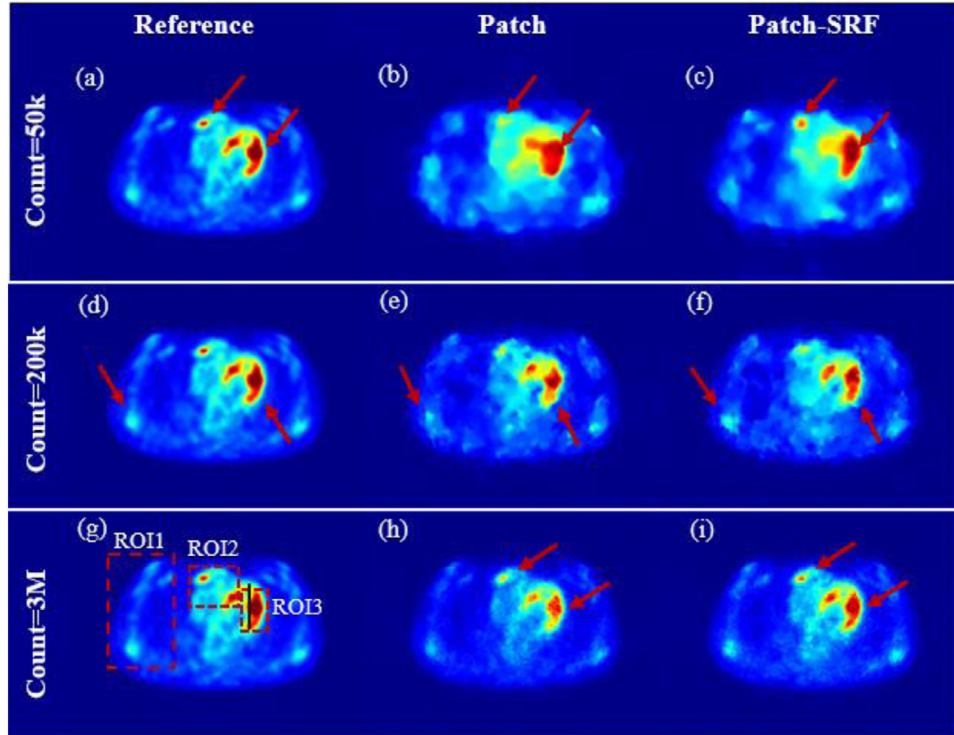


Fig. 1. The experimental results of the three sets with different counting levels. (a) Original axial PET image. (b) Patch reconstruction result with a 50k count level. (c) Image reconstructed with the proposed algorithm with a 50k count level. (d) Original axial PET image. (e) Patch reconstruction result with a 200k count level. (f) Image reconstructed with the proposed algorithm with a 200k count level. (g) Original axial PET image. (h) Patch reconstruction result with a 3M count level. (i) Image reconstructed with the proposed algorithm with a 3M count level. All the images are displayed in the same window.

quality and is more similar to the reference PET image than the patch reconstruction result.

5. Conclusion

In this work, we proposed a novel method that uses random forests to perform super-resolution (SR) processing at each iteration of the reconstruction step in the sinogram domain and the image domain. We proposed such a method because selectively performing the super-resolution reconstruction after each iteration allows the reconstruction to converge in advance and bypasses the time-intensive process of

parameter adjustment. Consequently, better reconstruction results can be achieved under relatively poor parameter settings.

This study has some limitations. We only carried out experiments on two-dimensional PET images to verify the feasibility of the algorithm. Since the clinical sinogram data could not be obtained, we were only able to conduct experimental simulations without any physical experiments. These simulations showed that the quality of the image reconstructed using the proposed algorithm was both qualitatively and quantitatively superior to the patch reconstruction. Please note that these experimental results are preliminary, and we will conduct future experiments testing the proposed algorithm clinically on three-dimensional PET images.

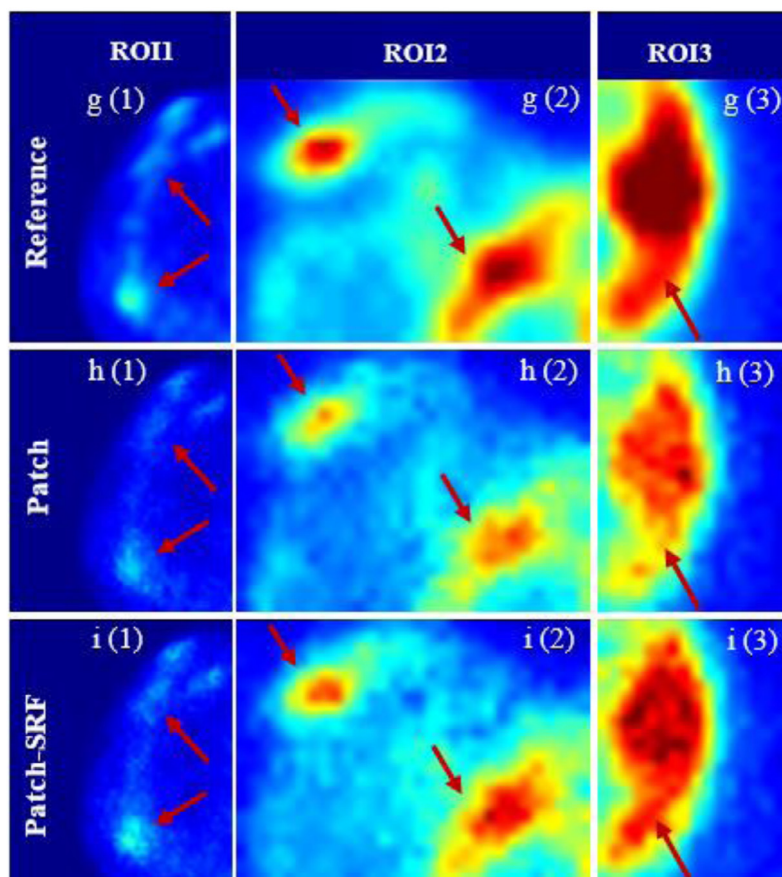


Fig. 2. The partial enlargement of Fig. 1(g)–(i).

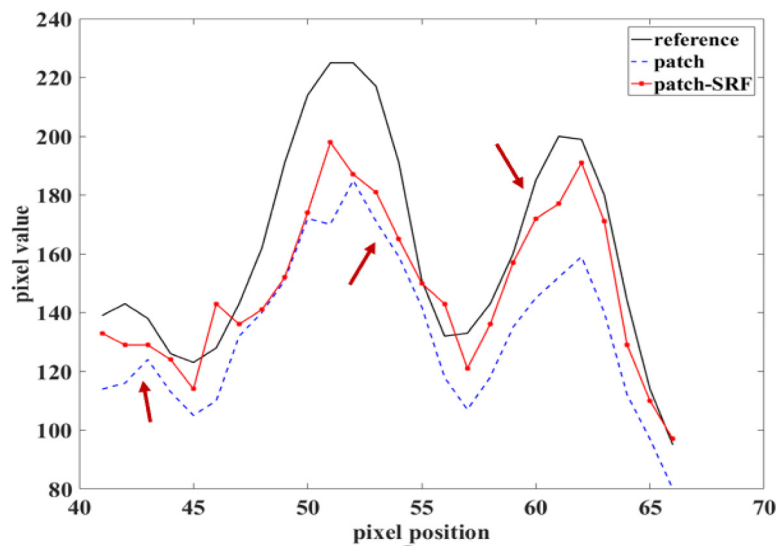


Fig. 3. The profile of the black line marked in Fig. 1(g) for the 3M count level results.

Acknowledgments

The authors would like to thank the editor and anonymous reviewers for their constructive comments and suggestions. This work was supported by the National Natural Science Foundation of China

(81871441), the Guangdong International Science and Technology Cooperation Project of China (2018A050506064), the Natural Science Foundation of Guangdong Province in China (2017A030313743), the Guangdong Special Support Program of China (2017TQ04R395), and the Chinese Academy of Sciences Key Laboratory of Health Informatics in China (2011DP173015). The authors would also like to thank

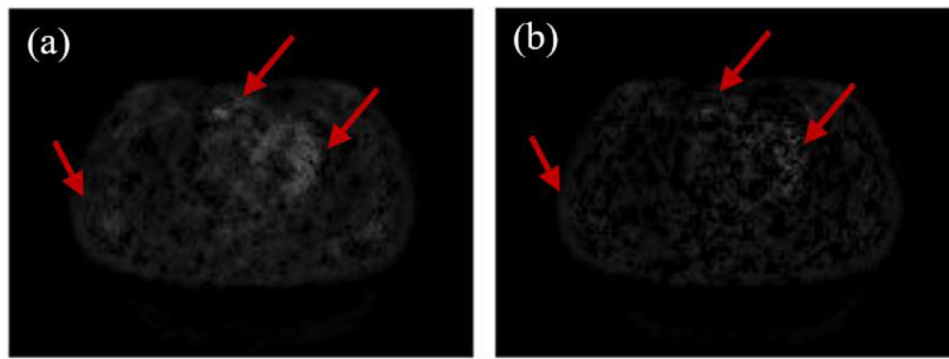


Fig. 4. The residual images of the patch reconstruction and the proposed algorithm compared to the reference at a 3M count level. (a) The residual image of the reference and the patch results. (b) The residual image of the reference and the results of the proposed algorithm. All the images are displayed in the same window.

Professor Xiaohua Zhu, of Tongji Hospital, Tongji Medical College, and Huazhong University of Science & Technology, for providing clinical data.

References

- [1] A. Soluri, G. Atzeni, A. Ucci, T. Bellone, F. Cusanno, G. Rodilossi, R. Massari, New device based on the super spatial resolution (SSR) method, *Nucl. Instrum. Methods A* 728 (2013) 150–156.
- [2] M. Madsen, *Emission Tomography: the Fundamentals of PET and SPECT*, 2005.
- [3] S. Tong, A.M. Alessio, P.E. Kinahan, Image reconstruction for PET/CT scanners: past achievements and future challenges, *Imaging Med.* 2 (2010) 529–545.
- [4] S. Muraro, N. Camarlinghi, G. Battistoni, N. Belcari, M.G. Bisogni, L. Cristoforetti, A. Del Guerra, A. Ferrari, F. Fracchiolla, A. Kraan, M. Morrocchi, R. Righetto, P. Sala, M. Schwarz, G. Sportelli, A. Topi, V. Rosso, Low statistics positron activity reconstruction methods for proton therapy, *Nucl. Instrum. Methods Phys. Res. A* 936 (2019) 52–53.
- [5] L. Caldeira, J. Scheins, P. Almeida, H. Herzog, Evaluation of two methods for using MR information in PET reconstruction, *Nucl. Instrum. Methods Phys. Res. A* 702 (2013) 141–143.
- [6] Y. Meng, P. Yan, H. Hui, J. Li, Filtered back projection reconstruction research based on Gaussian in PET images, in: *International Conference on Audio*, 2012.
- [7] M. DeFrise, Image reconstruction algorithms in PET, *Positron emission tomography*, in: *Basic Science and Clinical Practice*, 2003, pp. 91–114.
- [8] M. Tohme, *Iterative Image Reconstruction for Positron Emission Tomography Based on Measured Detector Response Function* (Dissertations & theses-Gradworks), 2011.
- [9] J.E. Ortuño, P. Guerra-Gutiérrez, J.L. Rubio, G. Kontaxakis, A. Santos, 3D-OSEM iterative image reconstruction for high-resolution PET using precalculated system matrix, *Nucl. Instrum. Methods Phys. Res. A* 569 (2006) 440–444.
- [10] M.E. Daube-Witherspoon, G. Muehllehner, An iterative image space reconstruction algorithm suitable for volume ECT, *IEEE Trans. Med. Imaging* 5 (1986) 61–66.
- [11] B.A. Anderson, M. Mair, J.M. Rao, C.H. Wu, Weighted least-squares reconstruction methods for positron emission tomography, *IEEE Trans. Med. Imaging* 16 (1997) 159.
- [12] J.M.M. Anderson, B.A. Mair, Accelerated penalized weighted least-squares and maximum likelihood algorithms for reconstructing transmission images from PET transmission data, *IEEE Trans. Med. Imaging* 24 (2005) 337–351.
- [13] F.L. Vermeulen, On the performance of maximum-likelihood reconstructions in positron emission tomography, *Proc. SPIE - Int. Soc. Opt. Eng.* 397 (1983) 274–279.
- [14] L.A. Shepp, Y. Vardi, Maximum likelihood reconstruction for emission tomography, *IEEE Trans. Med. Imaging* 1 (1982) 113–122.
- [15] G. Kontaxakis, Maximum likelihood image reconstruction in positron emission tomography (PET): Convergence characteristics and stopping rules, *Med. Phys.* 24 (1997) 1335.
- [16] J.A. Fessler, A.O. Hero, Penalized maximum-likelihood image reconstruction using space-alternating generalized EM algorithms, *IEEE Trans. Image Process.* 4 (1995) 1417–1429.
- [17] A. Sangtae, J.A. Fessler, B. Doron, A.O. Hero, Convergent incremental optimization transfer algorithms: application to tomography, *IEEE Trans. Med. Imaging* 25 (2006) 283.
- [18] C. Ji-Ho, J.M.M. Anderson, J.R. Votaw, Regularized image reconstruction algorithms for positron emission tomography, *IEEE Trans. Med. Imaging* 23 (2004) 1165.
- [19] S. Matej, J.A. Fessler, I.G. Kazantsev, Iterative tomographic image reconstruction using fourier-based forward and back-projectors, in: *Nuclear Science Symposium Conference Record*, 2002.
- [20] A.R. De Pierro, M.E. Belezia Yamagishi, Fast EM-like methods for maximum a posteriori estimates in emission tomography, *IEEE Trans. Med. Imaging* 20 (2001) 280–288.
- [21] M.I. Miller, B. Roysam, Bayesian image reconstruction for emission tomography incorporating good's roughness prior on massively parallel processors, *Proc. Natl. Acad. Sci. USA* 88 (1991) 3223–3227.
- [22] H.S. Hou, H.C. Andrews, Cubic splines for image interpolation and digital filtering, *IEEE Trans. Acoust. Speech Signal Process.* 26 (1978) 508–517.
- [23] P. Xia, T. Tahara, T. Kakue, Y. Awatsuji, K. Nishio, S. Ura, T. Kubota, O. Matoba, Performance comparison of bilinear interpolation, bicubic interpolation, and B-spline interpolation in parallel phase-shifting digital holography, *Opt. Rev.* 20 (2013) 193–197.
- [24] Y. Jianchao, W. John, H. Thomas, M. Yi, Image super-resolution via sparse representation, *IEEE Trans. Image Process.* 19 (2010) 2861–2873.
- [25] R. Zeyde, M. Elad, M. Protter, On Single Image Scale-Up using Sparse-Representations, Springer, Berlin, Heidelberg, 2012, pp. 171–730.
- [26] L. Breiman, Random forests, *Mach. Learn.* 45 (2001) 5–32.
- [27] S. Schuler, C. Leistner, H. Bischof, Fast and accurate image upscaling with super-resolution forests, *Comput. Vis. Pattern Recognit.* (2015).
- [28] Z.L. Hu, Y. Wang, X.Z. Zhang, M.X. Zhang, Y.F. Yang, X. Liu, H.R. Zheng, D. Liang, Super-resolution of PET image based on dictionary learning and random forests, *Nucl. Instrum. Methods A* 927 (2019) 320–329.
- [29] D. Chao, C.L. Chen, K. He, X. Tang, Learning a Deep Convolutional Network for Image Super-Resolution, 2014.
- [30] C. Dong, C.C. Loy, K. He, X. Tang, Image super-resolution using deep convolutional networks, *IEEE Trans. Pattern Anal. Mach. Intell.* 38 (2016) 295–307.
- [31] J. Kim, J.K. Lee, K.M. Lee, Deeply-recursive convolutional network for image super-resolution, in: *Proc CVPR IEEE*, 2016, pp. 1637–1645.
- [32] W. Guobao, Q. Jinyi, Penalized likelihood PET image reconstruction using patch-based edge-preserving regularization, *IEEE Trans. Med. Imaging* 31 (2012) 2194–2204.
- [33] M. Li, Generalized Lagrange multiplier method and KKT conditions with an application to distributed optimization, *IEEE Trans. Circuits Syst. II Express Briefs* 66 (2019) 1.
- [34] M. Dahlbom, Estimation of image noise in PET using the bootstrap method, *IEEE Trans. Nucl. Sci.* 49 (2002) 2062–2066.